Nature and timing of anatectic event of the Hida Belt (Japan): Constraints from titanite geochemistry and U-Pb age of clinopyroxene-bearing leucogranite

Hironobu Harada[1], hironobu.harada.s7@dc.tohoku.ac.jp
Tatsuki Tsujimori[1,2], tatsukix@tohoku.ac.jp
Yoshiaki Kon[3], yoshiaki-kon@aist.go.jp
Shogo Aoki[4,5], s-aoki@gipc.akita-u.ac.jp
Kazumasa Aoki[4], kazumasa@das.ous.ac.jp

[1] Graduate School of Science, Tohoku University, Sendai 980-8578, Japan
[2] Center for Northeast Asian Studies, Tohoku University Sendai 980-8576, Japan
[3] Geological Survey of Japan, National Institute of Advanced Industrial Science and Technology, Tsukuba, Ibaraki 305-8567, Japan
[4] Department of Applied Science, Okayama University of Science, Okayama 700-0005, Japan
[5] Graduate School of International Resource Sciences, Akita University, Akita 010-8502, Japan

Corresponding author: Hironobu Harada

Abstract

The Hida Belt, central Japan, is a continental fragment, which was once a part of the crustal basement of the East Asian continental margin. It consists mainly of Permo-Triassic granite-gneiss complexes with both syn-to-late-metamorphic migmatite or granite bodies. Clinopyroxene-bearing leucogranite, locally called as 'Inishi'-type migmatite, occurs characteristically in the migmatite zone associated with amphibolite and marble. The leucogranite is characterized by the presence of coarse-grained diopside–hedenbergite series clinopyroxene and titanite in plagioclase-dominated matrix. Clinopyroxene contains abundant calcite inclusions. Euhedral titanite with high Th/U ratios (~2.8–7.8) and REE contents (~4514–14069 μg/g) contains polycrystalline 'granitic' inclusions. Those mineralogical features indicate the involvement of carbonate during anatexis. Considering a nominal pressure of 0.4–0.7 GPa of the Hida gneiss, Zr-in-titanite thermometry yields a temperature of 730–810 °C and 770–850 °C at a_{TiO2} = 0.5 and 1, respectively. The titanites show highly variable U/Pb ($^{238}U/^{206}Pb$ = 15.0–24.0) and Pb ($^{207}Pb/^{206}Pb$ = 0.172–0.419) isotope ratios, and the scattered trend follows a discordia line with a lower intercept at 225.4 ± 1.9 Ma. This titanite age would represent the timing of regional anatexis that have occurred in a later stage of the regional metamorphism of the Hida Belt. A high apparent thermal gradient at middle crustal levels might have caused by regional extension.

Keywords: titanite; leucogranite; U-Pb age; Hida Belt; Permo-Triassic tectonics

Introduction

The Hida Belt of central Japan (Fig. 1) is a continental fragment, which was once a part of the crustal basement of the East Asian continental margin prior to the opening of the Japan Sea in Miocene (e.g., Harada et al., 2021; Hiroi, 1981; Isozaki, 1997; Isozaki et al., 2010). The belt consists mainly of Permo-Triassic granite-gneiss complexes with migmatite, marble, calcareous gneiss, amphibolite, granitic gneiss and minor high aluminous pelitic schist (cf. Ehiro et al., 2016). Based on the lithological similarity and its geographical position, it has been postulated as a fragment of the North China Craton, which was affected by a Permo-Triassic regional metamorphism, coeval with a continental collision between the North China and South China cratons (e.g., Ernst et al., 2007; Isozaki, 1997; Isozaki et al., 2010; Oh et al., 2005). However, geological and tectonic correlation among the Hida Belt and Permo-Triassic collisional orogenic belts in East Asia remain controversial. After the pioneering SHRIMP (Sensitive High-Resolution Ion Microprobe) work by Sano et al. (2000), ion microprobe and LA-ICPMS zircon U-Pb data has been accumulated in the Hida Belt during the last decade (Cho et al., 2021; Horie, et al., 2010, 2018; Takahashi et al, 2010, 2018; Takehara and Horie, 2019; Takeuchi et al., 2019; Yamada et al., 2021). Thus far, regional upper amphibolite- to granulite-facies metamorphism and related igneous activity have been dated as ~260–230 Ma.

In the Hida Belt, the regional anatectic event results in the formation of the clinopyroxene-bearing leucogranite in the migmatite zone, locally called as 'Inishi'-type migmatite (e.g., Kano, 1992; Sakoda et al., 2006). The leucogranite generally occurs in association with amphibolite, orthogneiss, calcareous gneiss and marble and often contains xenolith of those rocks (Kano et al., 1992). Since the leucogranite occurs closely associated with marble, it is suggested that the involvement of marble to their formation (Kunugiza et al., 2010). In any case, cross-cutting field relationships between the gneissose rocks and leucogranites indicate that the anatexis has occurred at a later stage of the regional metamorphism. Although SHRIMP zircon U-Pb dating of the leucogranite yields a concordant age of 234.5 ± 2.1 Ma (Sakoda et al., 2006), the zircon U-Pb ages might be inherited from their protolith prior to the regional anatexis. In fact, U-Pb ages of the zircons show a wide range from 266.4 Ma to 225.8 Ma (Sakoda et al., 2006).

In this study, we focused on titanite of the leucogranite to constrain the nature and timing of the regional anatectic event. We describe inclusion mineralogy and trace-element geochemistry of both titanite and clinopyroxene in the leucogranite, and we also present a titanite U-Pb age that represents the timing of the regional anatexis.

Geological background

Tectonic sketch of East Asia

Continental lithosphere of East Asia, located in eastern part of the Eurasian Continent, was formed after the amalgamation of several continental and micro-continental blocks; major cratonic blocks include the North China Craton (NCC) and the South China Craton (SCC). The convergent plate motion beginning early-Paleozoic generated a continental arc along the margin of the Cathaysia Block of SCC, and the collision between the NCC and SCC generated the Sulu–Dabie orogen, along the paleo-Pacific edge of cratonal Asia. The Sulu–Dabie orogen of East China has received the most intensive investigations as the UHP terrane since early 90s. Blocks, boudins and layers of eclogite and garnet peridotite occur as enclaves in quartzo-feldspathic gneisses. Ubiquitous occurrences of coesite inclusions in zircons of felsic gneisses and eclogites indicate that the supracrustal rocks were subducted to depths >100 km (e.g., Liou et al., 2009; 2014). The collisional suture may go to metamorphic complex of the Korean Peninsula (Oh, 2006), which consists of at least three polymetamorphosed Precambrian basement unit with Permo-Triassic metamorphic and magmatic records and Barrovian style metamorphic belts (Cho et al, 2007) (Figs. 1 and 2).

It is natural that some geotectonic units of East Asia should connect to the Japanese Islands. The Japanese Islands contain a long active Pacific-type accretionary orogens, that was formed by subduction, oceanward-accretion, and landward-erosion, which began in the early-Paleozoic (e.g., Isozaki, 1997; Isozaki et al., 2010; Pastor-Galán et al., 2021). Pre-Cretaceous geotectonic units of the Japanese Islands have been considered to have grown along the Cathaysia Block of the SCC margin ('Greater South China': e.g., Isozaki, 2019). The Japanese accretionary-related units also correlate to the Far Eastern Russia (e.g., Ishiwatari and Tsujimori, 2003). However, some fragments of 'non-accreted' origin basement rocks exist locally in Japan. The Hida Belt of central Japan is granitic gneiss and granite-dominant low-pressure and high-temperature type metamorphic belt that significantly differs from the other accretionary-related units of Japan (Isozaki, 1997). The gneissose rocks contain abundant ~1.8 Ga magmatic zircons and some Archean zircons (Horie et al., 2010, 2018; Sano et al., 2000). Based on U-Pb ages and Hf isotope compositions of zircons from orthogneiss, Cho et al. (2021) proposed a geotectonic correlation between the Hida Belt and the Yeongnam Massif of the Korean Peninsula.

Geological setting of the Hida Belt

Major exposures of upper amphibolite- to granulite-facies gneissose rocks of the Hida Belt are located in Kamioka, Odorigawa and Wadagawa areas. Minor pelitic gneiss contains sillimanite, garnet and biotite with very rare staurolite (e.g., Asami and Adachi, 1976; Jin and Ishiwatari, 1997). These gneissose rocks are unconformably covered by the Cretaceous Tetori Group sediments with some clasts derived from the basement (e.g., Sano and Yabe, 2017; Tsujimori, 1995). Geochronological studies revealed that the timing of the regional metamorphic event is ~260–230 Ma (e.g., Cho et al., 2021; Horie et al., 2018; Takahashi et al., 2018).

Granitic rocks (including their metamorphic equivalents) of the Hida Belt have been grouped into two types: older mostly deformed granites of ~260–230 Ma and younger undeformed granites of ~200–180 Ma (Kano, 1990a, b; Takahashi et al., 2010; Yamada et al., 2021). There are two remarkable peaks on the zircon U-Pb concordant age data of igneous and metamorphic rocks from the Hida Belt in the literature (Fig. 2): the Permo-Triassic regional metamorphic event and older granitic activity of ~260–230 Ma, and younger granitic intrusions of ~200–180 Ma.

The Kamioka area (Fig. 1c) is a well-mapped area, where the Pb-Zn ore deposit Kamioka Mine is located. The overall structure shows NS to NE–SW axis fold structure with wavelength of 1–2 km (Kano, 1982; Sohma and Akiyama, 1984). This area consists of granitic and metamorphic rocks such as migmatite, marble, calcareous gneiss and amphibolite. Gneissose and granitic rocks thrust over the Mesozoic Tetori Group sediments at the northern part of the Kamioka area. The eastern and southern parts of the area are mainly composed of granitic rocks. The Funatsu Shear Zone, which consists of mylonitic granite and augen gneiss, is located between gneissose rocks and granitic rocks (e.g., Kano, 1983; Komatsu et al., 1993). The SHRIMP U-Pb zircon dating of the deformed and undeformed granitic rocks suggests that the mylonitization occurred between 240 Ma and 199 Ma (Takahashi et al., 2010; Takehara and Horie, 2019). The younger granite intruded into the older granite, and a hornfels-like texture of the older granitic rocks at the boundary suggests a contact metamorphism by the younger granitic intrusions (Kano and Watanabe, 1995).

The clinopyroxene-bearing leucogranite occurs characteristically in the migmatite zone and contains coarse-grained clinopyroxene and titanite in a medium to coarse-grained plagioclase-dominated matrix. The leucogranite generally contains amphibolite, orthogneiss, marble and calcareous gneiss xenoliths (Kano, 1992). It is postulated that the leucogranite is formed by the interaction between granitic magma and marble (Kunugiza et al., 2010). The lithology and chemical compositions of the leucogranite are highly heterogeneous; modal compositions of the leucogranite vary from dioritic to granitic or syenitic, mostly dioritic and quartz dioritic compositions (Kano, 1981, 1992). The leucogranite consists mainly of plagioclase, quartz, diopside–hedenbergite series clinopyroxene ([Mg/(Mg + Fe)] = 0.40–0.70, mostly 0.50–0.60) and various content of alkali feldspar, and it characteristically contains coarse-grained titanite (Kano, 1992).

The investigated leucogranite was collected in a river bench of the Takahara River, Kamioka area, Gifu Prefecture (Fig. 1c). The leucogranite is coarse-grained and contains amphibolite xenoliths (Fig. 3).

Petrography and sample description

Leucogranite

The investigated leucogranite consists mainly of plagioclase (~55 vol.%), quartz (~15%), alkali feldspar (~10%), clinopyroxene (~15%), with small amount of titanite (~1%), amphibole and secondary chlorite. Apatite, calcite, prehnite (secondary), allanite, Fe-oxide and Fe-sulfide are accompanied as accessories. Titanite occurs as euhedral crystals up to 1 cm in length (Figs. 3 and 4a,b,d). Titanite crystals contain micrometer-sized polycrystalline 'granitic' inclusions (Fig. 4e,f) which consist of hypidiomorphic aggregate of quartz, plagioclase, alkali feldspar, epidote, minor allanite, calcite and apatite; chlorite occurs as secondary phase. Clinopyroxene occurs mainly as subhedral to euhedral crystals up to several cm in size (Fig. 4a,c), and it occurs as fine-grained crystals at the contact between the amphibolite xenoliths and leucogranite (Fig. 3c,d). The clinopyroxene contains quartz, plagioclase and titanite inclusions. Very fine-grained mineral inclusions were also identified with a laser Raman spectrometer, HORIBA JOBIN YVON LabRAM300 at Tohoku University, using a 488 nm line of solid-state laser at 25 mW. The Raman analysis found abundant calcite inclusions in clinopyroxene (Fig. 5).

Amphibolite xenolith

Weakly foliated amphibolite (Fig. 3c) consists mainly of brown amphibole (up to 1.5 mm in size), plagioclase, with small amount of ilmenite and apatite (Fig. 4g). Brown amphibole has tschermakitic and pargasitic compositions with Si = 6.03–6.53 p.f.u. (O = 23), $^{[A]}$(Na+K) = 0.28–0.64 p.f.u. and high K content (0.24–0.32 p.f.u.). Coarse-grained amphibolite (Fig. 3d) consists mainly of coarse-grained brown amphibole (up to 1.5 cm in size), plagioclase, with small amount of ilmenite, magnetite and apatite (Fig. 4h). Brown amphibole has a tschermakitic composition with Si = 6.10–6.26 p.f.u., and it has high Ti content (0.18–0.30 p.f.u.).

Trace-element chemistry

In-situ trace elements analysis was carried out with an Agilent 8900cx single-collector quadrupole ICP-MS coupled to a Cyber Laser TiS: femtosecond laser ablation (LA) system at the Geological Survey of Japan. The samples were set in a T201K sample cell of the LA system, and a Shardis static mixer (Y-20A-8E, Younitech Co., Ltd.) was connected between LA system and ICP-MS to stabilize a signal (Kon et al., 2020). The laser ablation was conducted at the condition of wavelength of 260 nm, fluence of 25 J/cm^2 repetition rate of 20 Hz, and ablation time of 20 s. Spot size of an ablation crater was 30 μm by whirlpool rastering of φ10 μm laser probe. On the ICP-MS, 51 nuclides (^{7}Li, ^{23}Na, ^{24}Mg, ^{27}Al, ^{28}Si, ^{31}P, ^{39}K, ^{40}Ca, ^{45}Sc, ^{49}Ti, ^{51}V, ^{52}Cr, ^{55}Mn, ^{56}Fe, ^{59}Co, ^{60}Ni, ^{63}Cu, ^{66}Zn, ^{69}Ga, ^{85}Rb, ^{88}Sr, ^{89}Y, ^{90}Zr, ^{93}Nb, ^{133}Cs, ^{137}Ba, ^{139}La, ^{140}Ce, ^{141}Pr, ^{146}Nd, ^{147}Sm, ^{151}Eu, ^{153}Eu, ^{157}Gd, ^{159}Tb, ^{163}Dy, ^{165}Ho, ^{166}Er, ^{169}Tm, ^{172}Yb, ^{175}Lu, ^{178}Hf, ^{181}Ta, ^{182}W, ^{204}Pb, ^{205}Tl, ^{206}Pb, ^{207}Pb, ^{208}Pb, ^{232}Th, and ^{238}U) were analyzed by H_2

reaction mode. The NIST SRM 610 and BCR-2G were analyzed as calibration standards for correcting sensitivity factors (Jochum and Nohl, 2008; Jochum et al., 2011).

The major and trace element data of the 83 analyzed spots of two titanite crystals, 23 spots of two clinopyroxene crystals, 20 spots of two plagioclase crystals and 20 spots of one alkali feldspar crystal in the leucogranite are shown in Figure 6a-d and Supplementary Table 1.

Titanite contains ~43–107 μg/g Sr, ~369–1440 μg/g Y, ~26–144 μg/g Th, ~8–27 μg/g U, ~0.5–8 μg/g Pb, ~352–954 μg/g Nb, ~19–60 μg/g Ta and ~537–1134 μg/g Zr. It shows high Th/U ratios (~2.8–7.8). Total REE concentrations (~4514–14069 μg/g) are two or three orders of magnitude larger than those of clinopyroxene (~6–45 μg/g). Trace element abundances vary one order of magnitude within a grain. Most trace elements do not show clear systematic core-to-rim profiles, whereas HREE is slightly enriched at the rim. The CI-chondrite-normalized REE patterns of titanite (Fig. 6a) show enrichment in LREE with smooth depletion of HREE and negative Eu anomaly.

Clinopyroxene (Mg# [= Mg/(Mg + Fe^{2+})] = 0.41–0.48) contains ~25–48 μg/g Sr, ~2–8 μg/g Y, ~4–19 μg/g Zr and up to ~12.5 μg/g Pb. It has LREE-enriched and flat HREE patterns with negative Eu anomaly (Fig. 6b). Comparing to trace element compositions of clinopyroxenes with a similar Mg# from the high-fractionated, plagioclase-clinopyroxene cumulates of the Skaergaard Intrusion (Namur and Humphreys, 2018), clinopyroxenes from our leucogranite are characterized by low REE and high Sr concentrations.

Plagioclase ($An_{27–35}$) has ~1173–1474 μg/g Sr, ~12–659 μg/g Ba, ~0.3–4 μg/g Ce, ~0.2–0.8 μg/g Eu and ~4–17 μg/g Pb. It tends to show lower REE rather than that of similar plagioclase ($An_{\sim30}$) in the Skaergaard plagioclase-clinopyroxene cumulates (Namur and Humphreys, 2018). Alkali feldspar contains ~267–299 μg/g Rb, ~891–1267 μg/g Sr, ~5–8 μg/g Cs, ~3150–4365 μg/g Ba, ~0.2–0.8 μg/g Eu and ~33–47 μg/g Pb.

Titanite U-Pb dating

In-situ titanite U-Pb dating was carried out with a Thermo Fisher Scientific iCAP-RQ single-collector quadrupole coupled to a Teledyne Cetac Technologies Analyte G2 ArF excimer LA system at the Okayama University of Science. The samples were set in a two-volume HelEx2 sample cell of the LA system. The laser ablation was conducted at the condition of laser spot size of 65 μm, fluence of 5 J/cm^2 and repetition rate of 10 Hz. On the ICP-MS, 5 nuclides (^{202}Hg, ^{204}Pb, ^{206}Pb, ^{207}Pb and ^{238}U) were analyzed. The BLR-1 titanite (Aleinikoff et al., 2007) was analyzed as a calibration standard for correcting mass bias of Pb/U ratios, and NIST SRM 612 was analyzed for Pb/Pb isotopic ratios. All uncertainties are quoted at a 2-sigma level to which repeatability of measurements of primary standards are propagated based on quadratic addition. Further details of our titanite U-Pb analysis method are given in Aoki and Aoki (2020). The MKED-1 (Spandler et al., 2016) was analyzed as the secondary standard with the unknown titanites. Weighted mean ^{207}Pb-^{206}Pb, ^{238}U-^{206}Pb and ^{235}U-^{207}Pb ages with 2σ uncertainties of 1523.2 ± 3.3 Ma (MSWD = 1.1), 1523.0 ± 13 Ma (MSWD = 0.11) and 1522.9 ± 7.6 Ma (MSWD = 0.14) were obtained from the MKED-1 (n = 9), which are consistent with the reference ^{207}Pb-^{206}Pb, ^{238}U-^{206}Pb and ^{235}U-^{207}Pb ages of 1521.02 ± 0.55 Ma, 1518.87 ± 0.31 Ma and 1517.32 ± 0.32 Ma by the ID-TIMS (Spandler et al., 2016).

Seventy-four U-Pb analyses were performed on 5 titanite grains. The results of titanite U-Pb data are shown in Table 1 and plotted on a Tera–Wasserburg Concordia diagram (Fig. 7). Titanite typically contains a relatively large amount of common lead, but provided there is a sufficient spread in the proportion of radiogenic to common Pb, the lower intercept of the discordia line determines a crystallization age, which is equivalent to a common Pb correction. Analyzed titanites show highly variable ^{238}U/^{206}Pb ratio (15.0–24.0) and ^{207}Pb/^{206}Pb ratio (0.172–0.419). Seventy-four spot isotope analyses define a discordia in the concordia diagram, yielding a lower intercept age of 225.4 ± 1.9 Ma (MSWD = 3, *n* = 74). Although the MSWD value is high, individual calculations for each sample show low values; MSWD for lower intercept ages of grain-1 (223.9 ± 7.8 Ma), grain-2 (232.4 ± 14.0 Ma), grain-3 (225.3 ± 4.7 Ma), and grain-4 (231.6 ± 4.1 Ma) are 1.9 (*n* = 15), 1.3 (*n* = 14), 1.9 (*n* = 15), 2.3 (*n* = 15) and 1.6 (*n* = 15), respectively.

Discussion

Origin of leucogranite

It has been known that amphibolite melting can generate silicic melt to form leucosomes (e.g., Brophy, 2008; Pu et al., 2014). As shown in geological map (Fig. 1c), the distribution of clinopyroxene-bearing leucogranite is closely associated with marble. Although the investigated leucogranite does not contain xenoliths of marble, the presence of abundant calcite inclusions in clinopyroxene supports carbonate-involved dehydration melting of amphibolite.

As described above, the euhedral shape of titanite crystals and the presence of polycrystalline 'granitic' inclusions (Fig. 4e,f) indicate that titanites in the clinopyroxene-bearing leucogranite crystalized from the anatectic melt. The origins of titanite are also distinguished by trace element features. In general, magmatic titanite is characterized commonly by high REE content and Th/U values compared to metamorphic titanite (e.g., Aleinikoff et al., 2002; Gao et al, 2012; Li et al., 2010). By using these features, Chen and Zheng (2015) and Chen et al. (2016) distinguished the anatectic domain from the metamorphic domain, and they showed the anatectic titanite which had grown from hydrous melts showed similar characteristics to the magmatic titanite. Our titanite data show high Th/U ratios (~2.8–7.8), and this feature strongly suggests a melt involved crystallization. Although the REE contents of analyzed titanites overlap to some of the metamorphic titanites found in the literature, they can be distinguished from metamorphic titanite in a Th/U vs. total REE plot (Fig. 6e). The titanites in the leucogranite can be also distinguished from the metamorphic titanite based on their La/Yb ratios (Fig. 6f). In conclusion, trace element compositions of investigated titanite support the crystallization from the anatectic melt.

Polycrystalline 'granitic' inclusions in analyzed titanites contain epidote. In general, the occurrence of magmatic epidote depends on the oxygen fugacity and the chemical compositions of melt (e.g., Schmidt and Thompson, 1996). It is also suggested that magmatic epidote in granitic melt systems tends to have formed at moderate pressure (~0.5–0.8 GPa) conditions (e.g., Masumoto et al., 2014; Naney, 1983; Zen and Hammarstrom, 1984). The presence of epidote in the 'granitic' inclusions in titanite crystals is consistent with the anatexis at mid-crustal conditions.

Using experimentally determined trace-element partition coefficients between silicate melt and titanite and/or diopside, the compositions of the anatectic melt can be estimated. According to Prowatke and Klemme (2005), partitioning of some elements (Nb, Ta, Th, U and REE) depends highly on the compositions of silicate melt, especially the alumina saturation index (ASI: molar ratio $Al_2O_3/(Na_2O + K_2O + CaO)$). Since the leucogranite contains abundant plagioclase, it should have high ASI value (ASI > 0.5: Kano, 1992). Thus, we applied silicate melt–titanite partitioning data for five different melt compositions of Prowatke and Klemme (2005) (ASI > 0.5). In addition, we applied silicate melt–diopside partition coefficients for Na_2O bearing anorthite–diopside–titanite system (Shosnig and Hoffer, 1998). Estimated melt compositions are shown in Figure 8. Notably the Sr concentrations estimated from both titanite and diopside overlap with each other. Comparing with silicic melt generated by amphibolite melting (Pu et al., 2014), estimated melt compositions are high REE contents, especially LREE. Moreover, the inferred melt compositions are characterized by high U and Th content and

Nb/Ta ratio (Fig. 8b). These trace element features of estimated melt may reflect the involvement of carbonate during anatexis.

Condition of crustal anatexsis

We estimated the crystallization temperature of titanite using the Zr-in-titanite thermometry (Hayden et al., 2008). The thermometry requires the coexistence of quartz, rutile and zircon. Since rutile was not confirmed in the leucogranite, the TiO_2 activity cannot be regarded as 1. However, it was suggested that the plausible lower limits of the TiO_2 activity in most igneous and metamorphic rocks is about 0.5 (e.g., Ferry and Watson, 2007; Hayden and Watson, 2007). The pressure condition of the regional metamorphism on the Hida Belt is poorly constrained. The occurrence of the minor pelitic gneiss which contains sillimanite, garnet and biotite with very rare staurolite (Asami and Adachi, 1976) can constrain sillimanite and staurolite stability condition. A peak pressure condition of ~0.4–0.7 GPa summarized by Suzuki et al. (1989) seems to be reasonable and has been widely accepted as a nominal pressure of the regional metamorphism of the Hida Belt. Considering these, we calculated the TiO_2 activity for 0.5 and 1 at nominal pressure conditions of 0.4–0.7 GPa. Estimated temperature for a_{TiO2} = 0.5 and 1 are 730–810 °C and 770–850 °C, respectively (Fig. 9, Supplementary Table 2). Such high temperature crystallization is compatible with the titanite growth from anatectic melt.

Timing of the anatectic event in the Hida Belt

The U-Pb closure temperature of titanite is still unknown though different studies suggest the temperatures always over 600 ˚C (e.g., Gao et al., 2012; Scott and St-Onge, 1995; Spear and Parrish, 1996). For example, Scott and St-Onge (1995) suggested >~680 °C based on the titanite growth temperature. On the other hand, Gao et al. (2012) suggested >~800 °C from titanite samples which survived 800–850 °C metamorphism. Recent studies rather prefer such a high U-Pb closure temperature of > 830 °C (Hartnady et al., 2019; Kirkland et al., 2020). Even if U-Pb closure temperature of titanite is relatively low, our titanite crystals are large (3–5 mm in length), thus it is unlikely that coarse-grained titanite were influenced by intercrystalline Pb diffusion. Assuming the high closure temperature of titanite, titanite U-Pb age of 225.4 ± 1.9 Ma obtained from this study can be regarded as the timing of formation of the leucogranite, i.e., timing of the regional anatectic event.

Available zircon data suggest that the regional metamorphic event and coeval granitic activity of the Hida Belt was ~260–230 Ma (e.g., Cho et al., 2021; Horie et al., 2018; Sano et al., 2000; Takahashi et al., 2018). Our titanite U-Pb age corresponds to the ending time of an inferred regional metamorphic period of the Hida Belt (~260–230 Ma) (Fig. 10). In other words, the leucogranite-forming anatectic event might have occurred in a later stage of the regional metamorphism of the Hida Belt. However, this anatectic event can be clearly distinguished from the intrusion of younger granitic intrusions (~200–180 Ma). Considering new titanite U-Pb age of ~225 Ma and estimated titanite formation temperature of >700 °C at mid-crustal condition, the Hida Belt would have been at a high geothermal gradient in a later stage of the regional metamorphic activity of the Hida Belt. Such a high apparent geothermal gradient can be explained by a regional extension with the high heat flow from the upwelling of asthenospheric mantle (e.g., Sandiford and Powell, 1986; Zheng and Chen, 2017; Wickham and Oxburgh, 1985).

In the regional geotectonic context, it is reasonable to consider that all tectonic events recorded in the Hida Belt connect to its tectonic counterpart of East Asian margin (Fig. 1a). The 225 Ma anatectic event at a high geothermal gradient possibly due to regional extension can be a new key to correlate the Hida Belt to potential western counterparts in the Korean Peninsula. Nevertheless, to further our understanding of the geological correlation of the East

Asia continental margin, a more detailed and comprehensive approach is required than that documented in previous studies.

Acknowledgements

This research was supported by CNEAS of Tohoku University in part by grants from the MEXT/JSPS KAKENHI JP18H01299 to TT. This was also supported by MEXT Private University Research Branding Project (Okayama university of Science) to KA and JSPS KAKENHI JP19K04043 to KA. We are grateful for constructive comments from Chang-Whan Oh, Takeshi Imayama and anonymous reviewers, especially various suggestions from Chang-Whan Oh improved the paper significantly. We are grateful for constructive feedback from Daniel Pastor-Gálan. We extend our appreciation to Shunsuke Fukuhara, Hiroki Oka and Rio Higuchi for their field assistance.

Reference

Aleinikoff, J. N., Wintsch, R. P., Fannng, C. M., Dorais, M. J. 2002. U-Pb geochronology of zircon and polygenetic titanite from the Glastonbury Complex, Connecticut, USA: an integrated SEM, EMPA, TIMS, and SHRIMP study. Chemical Geology, 188, 125–147.

Aleinikoff, J. N., Wintsch, R. P., Tollo, R. P., Unruh, D. M., Fanning, C. M., Schmitz, M. D. 2007. Ages and origins of rocks of the Killingworth dome, south-central Connecticut: implications for the tectonic evolution of southern New England. American Journal of Science, 307, 63–118.

Aoki, S., Aoki, K. 2020. *In-situ* U-Pb age determination of titanite by LA-ICP-MS. Naturalistae, 24, 7–12.

Asami, M. Adachi, M. 1976. Staurolite-bearing cordierite-sillimanite gneiss from the Toga area in the Hida metamorphic terrane, central Japan. The Journal of the Geological Society of Japan, 82, 259–271.

Brophy, J. G. 2008. A study of rare earth element (REE)–SiO_2 variations in felsic liquids generated by basalt fractionation and amphibolite melting: a potential test for discriminating between the two different processes. Contributions to Mineralogy and Petrology, 156, 337–357.

Chen, Y. X., Zheng, Y. F. 2015. Extreme Nb/Ta fractionation in metamorphic titanite from ultrahigh-pressure metagranite. Geochimica et Cosmochimica Acta, 150, 53–73.

Chen, Y. X., Zheng, Y. F., Hu, Z. 2013. Polyphase growth of accessory minerals during continental collision: geochemical evidence from ultrahigh-pressure metamorphic gneisses in the Sulu orogen. Lithos, 177, 245–267.

Chen, Y. X., Zhou, K., Zheng, Y. F., Gao, X. Y., Yang, Y. H. 2016. Polygenetic titanite records the composition of metamorphic fluids during the exhumation of ultrahigh-pressure metagranite in the Sulu orogen. Journal of Metamorphic Geology, 34, 573–594.

Cho, D. L., Lee, T. H., Takahashi, Y., Kato, T., Yi, K., Lee, S., Cheong, A. C. S. 2021. Zircon U-Pb geochronology and Hf isotope geochemistry of magmatic and metamorphic rocks from the Hida Belt, southwest Japan. Geoscience Frontiers, 12, 101145.

Cho, M., Kim, Y., Ahn, J. 2007. Metamorphic evolution of the Imjingang belt, Korea: Implications for Permo-Triassic collisional orogeny. International Geology Review, 49, 30–51.

Ehiro, M., Tsujimori, T., Tsukada, K., Nuramkhaan, M. 2016. Paleozoic basement and associated cover: in Moreno, T, Wallis, S., Kojima, T., Gibbons, W. (eds.) The geology of Japan. Geological Society of London, pp. 25–60.

Ernst, W. G., Tsujimori, T., Zhang, R., Liou, J. G. 2007. Permo-Triassic collision, subduction-zone metamorphism, and tectonic exhumation along the East Asian continental margin. Annual Review of Earth and Planetary Science, 35, 73–110.

Ferry, J. M., Watson, E. B. 2007. New thermodynamic models and revised calibrations for the Ti-in-zircon and Zr-in-rutile thermometers. Contributions to Mineralogy and Petrology, 154, 429–437.

Fu, Y., Sun, X., Hollings, P., Li, D., Yang, T. 2018. Geochronology and trace element geochemistry of titanite in the Machangqing Cu-Mo-dominated polymetallic deposit, Yunnan Province, southwest China. Journal of Asian Earth Sciences, 158, 398–414.

Gao, X. Y., Zheng, Y. F., Chen, Y. X., Guo, J. 2012. Geochemical and U-Pb age constraints on the occurrence of polygenetic titanites in UHP metagranite in the Dabie orogen. Lithos, 136, 93–108.

Harada, H., Tsujimori, T., Kunugiza, K., Yamashita, K., Aoki, S., Aoki, K., Takayanagi, H., Iryu, Y. 2021. The $\delta^{13}C$–$\delta^{18}O$ variations in marble in the Hida Belt, Japan. Island Arc, 30, e12389.

Hartnady, M. I., Kirkland, C. L., Clark, C., Spaggiari, C. V., Smithies, R. H., Evans, N. J., McDonald, B. J. 2019. Titanite dates crystallization: Slow Pb diffusion during super-solidus re-equilibration. Journal of Metamorphic Geology, 37, 823–838.

Hayden, L. A., Watson, E. B. 2007. Rutile saturation in hydrous siliceous melts and its bearing on Ti-thermometry of quartz and zircon. Earth and Planetary Science Letters, 258, 561–568.

Hayden, L. A., Watson, E. B., Wark, D. A. 2008. A thermobarometer for sphene (titanite). Contributions to Mineralogy and Petrology, 155, 529–540.

Hiroi, Y. 1981. Subdivision of the Hida metamorphic complex, central Japan, and its bearing on the geology of the Far East in pre-Sea of Japan time. Tectonophysics, 76, 317–333.

Horie, K., Tsutsumi, Y., Takehara, M., Hidaka, H. 2018. Timing and duration of regional metamorphism in the Kagasawa and Unazuki areas, Hida metamorphic complex, southwest Japan. Chemical Geology, 484, 148–167.

Horie, K., Yamashita, M., Hayasaka, Y., Katoh, Y., Tsutsumi, Y., Katsube, A., Hidaka, H., Kim, H., Cho, M. 2010. Eoarchean–Paleoproterozoic zircon inheritance in Japanese Permo-Triassic granites (Unazuki area, Hida Metamorphic Complex): Unearthing more old crust and identifying source terrranes. Precambrian Research, 183, 145–157.

Ishiwatari, A., Tsujimori, T. 2003. Paleozoic ophiolites and blueschists in Japan and Russian Primorye in the tectonic framework of East Asia: A synthesis. Island Arc, 12, 190–206.

Isozaki, Y. 1997. Contrasting two types of orogen in Permo-Triassic Japan: Accretionary versus collisional. Island Arc, 6, 2–24.

Isozaki, Y. 2019. A visage of early Paleozoic Japan: Geotectonic and paleobiogeographical significance of Greater South China. Island Arc, 28, e12296.

Isozaki, Y., Aoki, K., Nakama, T., Yanai, S. 2010. New insight into a subduction-related orogen: A reappraisal of the geotectonic framework and evolution of the Japanese Islands. Gondwana Research, 18, 82–105.

Jin, F., Ishiwatari, A. 1997. Petrological and geochemical study on Hida gneisses in the upper reach area of Tetori river: Comparative study on the pelitic metamorphic rocks with the other areas of Hida belt, Sino-Korean block and Yangtze block. Journal of Mineralogy, Petrology and Economic Geology, 92, 213–230 (in Japanese with English abstract).

Jochum, K.P., Nohl, U. 2008. Reference materials in geochemistry and environmental research and the GeoReM database. Chemical Geology, 253, 50–53.

Jochum, K.P., Weis, U., Stoll, B., Kuzmin, D., Yang, Q., Raczek, I., Jacob, D.E., Stracke, A., Birbaum, K., Frick, D.A., Günther, D., Enzweiler, J. 2011. Determination of Reference

Values for NIST SRM 610–617 Glasses Following ISO Guidelines. Geostandards and Geoanalytical Research, 35, 397–429.
Kano, T. 1981. Migmatite structure of the Hida metamorphic region, central Japan. The Journal of Geological Society of Japan, 87, 315–328 (in Japanese with English abstract).
Kano, T. 1982. Tectonic divisions and their development of the Hida metamorphic region, central Japan. Memoirs of the Geological Society of Japan, 21, 9–24 (in Japanese with English abstract).
Kano, T. 1983. Origin of augen gneisses and related mylonitic rocks in the eastern part of the Hida metamorphic region, central Japan. (Part 1): Mode of occurrences, petrographical and mineralogical properties of rocks and potash-feldspar megacrysts. The Journal of the Geological Society of Japan, 89, 375–393 (in Japanese with English abstract).
Kano, T. 1990a. Intrusive relation of the Okumayama Granitic Mass (Shimonomoto type) into the Iori Granitic Mass (Funatsu type) in the Hayatsukigawa area: Re-examination of the sub-division for early Mesozoic granites (Funatsu Granites) in the Hida region. The Journal of Geological Society of Japan, 96, 379–388 (in Japanese with English abstract).
Kano, T. 1990b. Granitic rocks in the Hida complex, central Japan. Mining Geology, 40, 397–413 (in Japanese with English abstract).
Kano, T. 1992. Compositional variation of clinopyroxenes in so-called Inishi migmatitie and skarn ore (Mokuji Ore) in and around the Kamioka mining area, Japan. Mining Geology, 42, 379–390.
Kano, T., Watanabe, T. 1995. Geology and structure of the early Mesozoic granitoids in the east of the Kamioka mining area, southern Hida metamorphic region, central Japan. The Journal of Geological Society of Japan, 101, 499–514 (in Japanese with English abstract).
Kirkland, C. L., Yakymchuk, C., Gardiner, N. J., Szilas, K., Hollis, J., Olierook, H., Steenfelt, A. 2020. Titanite petrochronology linked to phase equilibrium modelling constrains tectono-thermal events in the Akia Terrane, West Greenland. Chemical Geology, 536, 119467.
Komatsu, M., Nagase, M., Naito, K., Kanno, T., Ujihara, M., Toyoshima, T. 1993. Structure and tectonics of the Hida massif, central Japan. Memoir of Geological Society of Japan, 42, 39–62 (in Japanese with English abstract).
Kon, Y., Yokoyama, T. D., Ohata, M. 2020. Analytical efficacy of gas-mixer and stabilizer for laser ablation-ICP mass spectrometry. ASC Omega, 5, 28073–28079.
Kunugiza, K., Shimizu, M., Otoh, S. 2010. U–Th–Pb chronological constraints on the geotectonic history of Central Japan from the Hida metamorphism through the opening of Japan to the present. Journal of the Geological Society of Japan, 116(Supplement), 83–101 (in Japanese).
Li, J. W., Deng, X. D., Zhou, M. F., Liu, Y. S., Zhao, X. F., Guo, J. L. 2010. Laser ablation ICP-MS titanite U-Th-Pb dating of hydrothermal ore deposits: a case study of the Tonglushan Cu-Fe-Au skarn deposit, SE Hubei Province, China. Chemical geology, 270, 56–67.
Liou, J. G., Ernst, W. G., Zhang, R. Y., Tsujimori, T., Jahn, B. M. 2009. Ultrahigh-pressure minerals and metamorphic terranes–the view from China. Journal of Asian Earth Sciences, 35, 199–231.
Liou, J. G., Tsujimori, T., Yang, J., Zhang, R. Y., Ernst, W. G. 2014. Recycling of crustal materials through study of ultrahigh-pressure minerals in collisional orogens, ophiolites, and mantle xenoliths: A review. Journal of Asian Earth Sciences, 96, 386–420.

Masumoto, Y., Enami, M., Tsuboi, M., Hong, M. 2014. Magmatic zoisite and epidote in tonalite of the Ryoke belt, central Japan. European Journal of Mineralogy, 26, 279–291.
McDonough, W. F., Sun, S. S. 1995. The composition of the Earth. Chemical geology, 120, 223–253.
Namur, O., Humphreys, M. C. S. 2018. Trace element constraints on the differentiation and crystal mush solidification in the Skaergaard intrusion, Greenland. Journal of Petrology, 59(3), 387–418.
Naney, M. T. 1983. Phase equilibria of rock-forming ferromagnesian silicates in granitic systems. American journal of science, 283, 993–1033.
Oh, C. W. 2006. A new concept on tectonic correlation between Korea, China and Japan: histories from the late Proterozoic to Cretaceous. Gondwana Research, 9, 47–61.
Oh, C. W., Kim, S. W., Choi, S. G., Zhai, M., Guo, J., Krishnan, S. 2005. First finding of eclogite facies metamorphic event in South Korea and its correlation with the Dabie-Sulu collision belt in China. The Journal of Geology, 113, 226–232.
Palin, R. M., White, R. W., Green, E. C., Diener, J. F., Powell, R., Holland, T. J. 2016. High-grade metamorphism and partial melting of basic and intermediate rocks. Journal of Metamorphic Geology, 34, 871–892.
Pastor-Galán, D., Spencer, C. J., Furukawa, T., Tsujimori, T. 2021. Evidence for crustal removal, tectonic erosion and flare-ups from the Japanese evolving forearc sediment provenance. Earth and Planetary Science Letters, 564, 116893.
Prowatke, S., Klemme, S. 2005. Effect of melt composition on the partitioning of trace elements between titanite and silicate melt. Geochimica et Cosmochimica Acta, 69, 695–709.
Pu, X., Brophy, J. G., Tsujimori, T. 2014. Rare earth element–SiO_2 systematics of island arc crustal amphibolite migmatites from the Asago body of the Yakuno Ophiolite, Japan: a field evaluation of some model predictions. Contributions to Mineralogy and Petrology, 168, 1060.
Richardson, S. W. 1968. Staurolite stability in a part of the system Fe-Al-Si-OH. Journal of Petrology, 9, 467–488.
Sakoda, M., Kano, T., Fanning, C. M., Sakaguchi, T. 2006. SHRIMP U-Pb zircon age of the Inishi migmatite around the Kamioka mining area, Hida metamorphic complex, Central Japan. Resource Geology, 56, 17–26.
Sakurai, W., Okada, Y., Mizuyachi, O. 1993. On the exploration of the Atotsugawa district in the Kamioka mining area, central Japan. Resource Geology, 43, 79–91 (in Japanese with English abstract).
Sandiford, M., Powell, R. 1986. Deep crustal metamorphism during continental extension: modern and ancient examples. Earth and Planetary Science Letters, 79, 151–158.
Sano, Y., Hidaka, H., Terada, K., Shimizu, H., Suzuki, M. 2000. Ion microprobe U-Pb zircon geochronology of the Hida gneiss: Finding of the oldest minerals in Japan. Geochemical Journal, 34, 135–153.
Sano, S. I., Yabe, A. 2017. Fauna and flora of Early Cretaceous Tetori Group in Central Japan: The clues to revealing the evolution of Cretaceous terrestrial ecosystem in East Asia. Palaeoworld, 26, 253–267.
Schmidt, M. W., Thompson, A. B. 1996. Epidote in calc-alkaline magmas: An experimental study of stability, phase relationships, and the role of epidote in magmatic evolution. American Mineralogist, 81, 462–474.
Schosnig, M., Hoffer, E. 1998. Compositional dependence of REE partitioning between diopside and melt at 1 atmosphere. Contributions to mineralogy and petrology, 133, 205–216.

Scott, D. J., St-Onge, M. R. 1995. Constraints on Pb closure temperature in titanite based on rocks from the Ungava orogen, Canada: Implications for U-Pb geochronology and P-T-t path determinations. Geology, 23, 1123–1126.
Sohma, T., Akiyama, S. 1984. Geological structure and lithofacies in the central part of the Hida metamorphic belt. The Journal of Geological Society of Japan, 90, 609–628 (in Japanese with English abstract).
Spear, F. S., Parrish, R. R. 1996. Petrology and cooling rates of the Valhalla complex, British Columbia, Canada. Journal of Petrology, 37, 733–765.
Spandler, C., Hammerli, J., Sha, P., Hilbert-Wolf, H., Hu, Y., Roberts, E., Schmitz, M. 2016. MKED1: A new titanite standard for *in situ* analysis of Sm-Nd isotopes and U-Pb geochronology. Chemical Geology, 425, 110–126.
Suzuki, M., Nakazawa, S., Osakabe, T. 1989. Tectonic development of the Hida Belt –with special reference to its metamorphic history and late Carboniferous to Triassic orogenies–. The Memoirs of the Geological Society of Japan, 33, 1–10 (in Japanese with English abstract).
Takahashi, Y., Cho, D. L., Kee, W. S. 2010. Timing of mylonitization in the Funatsu shear zone within Hida Belt of southwest Japan: Implications for correlation with the shear zones around the Ogcheon Belt in the Korean Peninsula. Gondwana Research, 17, 102–115.
Takahashi, Y., Cho, D. L., Mao, J., Zhao, X., Yi, K. 2018. SHRIMP U-Pb zircon ages of the Hida metamorphic and plutonic rocks, Japan: Implications for late Paleozoic to Mesozoic tectonics around the Korean Peninsula. Island Arc, 27, e12220.
Takehara, M., Horie, K. 2019. U-Pb zircon geochronology of the Hida gneiss and granites in the Kamioka area, Hida Belt. Island Arc, 28, e12303.
Takeuchi, M., Shibata, K., Jia, S., Yamamoto, K. 2019. U-Pb zircon ages of granitic rocks from Kagasawa, Hida Mountains. The Journal of Geological Society of Japan, 125, 453–459 (in Japanese with English abstract).
Thompson, A. B. 1982. Dehydration melting of pelitic rocks and the generation of H_2O-undersaturated granitic liquids. American Journal of Science, 282, 1567–1595.
Tsujimori, T. 1995. Staurolite-bearing sillimanite schist cobble from the Upper Jurassic Tetori Group in the Kuzuryu area, Hida Mountains, central Japan. The Journal of Geological Society of Japan, 101, 971–977.
Tsujimori, T. 2002. Prograde and retrograde P-T paths of the late Paleozoic glaucophane eclogite from the Renge metamorphic belt, Hida Mountains, southwestern Japan. International Geology Review, 44, 797–818.
Vermeesch, P. 2018. IsoplotR: A free and open toolbox for geochronology. Geoscience Frontiers, 9, 1479–1493.
Wickham, S. M., Oxburgh, E. R. 1985. Continental rifts as a setting for regional metamorphism. Nature, 318, 330–333.
Yamada, R., Sawada, H., Aoyama, S., Ouchi, W., Niki, S., Nagata, M., Takahashi, T., Hirata, T. 2021. Zircon U-Pb ages and whole–rock geochemistry from the Hida granites: implications for the geotectonic history and the origin of Mesozoic granites in the Hida belt, Japan. Journal of Mineralogical and Petrological Sciences, 116, 61–66.
Zen, E. A., Hammarstrom, J. M. 1984. Magmatic epidote and its petrologic significance. Geology, 12, 515–518.
Zheng, Y. F., Chen, R. X. 2017. Regional metamorphism at extreme conditions: Implications for orogeny at convergent plate margins. Journal of Asian Earth Sciences, 145, 46–73.

Table titles

Table 1. LA-ICPMS titanite U-Pb isotope data of titanite from the leucogranite (so-called 'Inishi'-type migmatite) of the Hida Belt.

Figure captions

Figure 1. (a) Tectonic framework of East Asia (modified after Harada et al., 2021). (b) Simplified geological map of the Hokuriku region, showing location of the Kamioka area (modified after Tsujimori, 2002). HG, Hida-Gaien Belt; Hd, Hida Belt; I.S.T.L., Itoigawa–Shizuoka Tectonic Line; M–T, Mino–Tamba Belt; Ry, Ryoke Belt. (c) A geological map of the Kamioka area, showing a sample locality (modified after Harda et al., 2021; Sakurai et al., 1993). Zircon U-Pb ages showing together with reference: [1] Clinopyroxene-bearing leucogranite (so-called 'Inishi'-type migmatite) collected from drill hole of Sakoda et al. (2006). [2] Banded gneiss of Takehara and Horie (2019). [3] Granitic mylonite of Takehara and Horie (2019). [4] Undeformed granite of Takehara and Horie (2019).

Figure 2. Summary of geochronological studies of basement rocks of the Hida Belt, North China Craton (Yinshan Block, Ordos Block, Eastern Block, Khondalite Belt, Trans-North China Orogen (TNCO) and Jiao-Liao-Ji Belt), Gyeonggi Massif, Yeongnam Massif, Sulu–Dabie Collision Belt, South China Craton (Yangtze Block, Cathaysia Block and Jiangnan Orogen) and Far Eastern Russia (Bureya, Jiamusi and Khanka terranes). References are shown in Supplementary material 1. A histogram shows SHRIMP and LA-ICPMS U-Pb age data from igneous and metamorphic rocks of the Hida Belt in the literature. Bin width of the histogram is 10 Myr.

Figure 3. (a) A photograph showing field view of the migmatite zone in the Hida Belt. The clinopyroxene-bearing leucogranite contains amphibolite xenoliths. (b) A typical appearance of the leucogranite. It contains coarse-grained clinopyroxene (Cpx) and titanite (Ttn). (c) Amphibolite xenolith in the leucogranite. (d) Coarse-grained amphibolite xenolith in the leucogranite. Abundant greenish clinopyroxene crystals occur near the boundary of two lithologies.

Figure 4. (a) A photograph showing an appearance of studied leucogranite (so-called 'Inishi'-type migmatite). The leucogranite contains coarse-grained clinopyroxene and titanite. (b) Crossed-polarized image (XPL) of coarse-grained euhedral titanite in leucogranite. (c) XPL image of leucogranite. (d) Plane–polarized light (PPL) image of titanite in leucogranite. (e) PPL image of polycrystalline 'granitic' inclusion in titanite. (f) Back-scattered electron (BSE) image of polycrystalline 'granitic' inclusion in titanite. (g) PPL image of weakly foliated amphibolite xenolith in leucogranite. (h) XPL image of coarse-grained amphibolite xenolith in leucogranite. This amphibolite is characterized by coarse-grained brown amphibole (up to 1.5 cm in size). Mineral abbreviations: Afs—alkali feldspar, Aln—allanite, Amp—amphibole, Ap—apatite, Chl—chlorite, Cpx—clinopyroxene, Ep—epidote, Ilm—ilmenite, Pl—plagioclase, Qz—quartz, Ttn—titanite, Zrn—zircon.

Figure 5. PPL image of calcite inclusion in clinopyroxene and Raman spectra of calcite (Cal) inclusions in clinopyroxene (Cpx). A spectrum of clinopyroxene is also shown for comparison.

Figure 6. (a)–(d) CI-chondrite normalized REEs and Primitive Mantle (PM)-normalized trace elements abundances of titanite and clinopyroxene in the leucogranite. (a) REE

patterns of titanite. (b) REE patterns of clinopyroxene, plagioclase and alkali feldspar. (c) Trace element patterns of titanite. (d) Trace element patterns of clinopyroxene, plagioclase and alkali feldspar. Both normalization factors are from McDonough and Sun (1995). (e) (f) Trace element characteristics of analyzed titanite. (e) The Th/U vs. total REE content (μg/g) plot. (f) The Th/U vs. La/Yb plot. Migmatite*—titanite crystalized from anatectic melt (Chen and Zheng, 2015; Chen et al., 2016). Metamorphic**—metamorphic titanite (Chen and Zheng, 2015; Chen et al., 2013; 2016; Gao et al., 2012). Magmatic***—magmatic titanite (Chen et al., 2013; Fu el al., 2018; Gao et al., 2012; Li et al., 2010).

Figure 7. Tera–Wasserburg Concordia diagram showing ~~of~~ all titanite U-Pb data. Seventy-four U-Pb isotope analyses define a discordia in the concordia diagram, yielding a lower intercept age of 225.4 ± 1.9 Ma. Data plotting and age calculation were performed using IsoplotR (Vermeesch, 2018).

Figure 8. (a) PM-normalized trace element patterns for titanite and clinopyroxene in the clinopyroxene-bearing leucogranite and inferred melt compositions estimated from titanite (pink domain) and diopside (gray domain). Melt compositions are calculated using silicate melt–diopside partition coefficients for Na_2O bearing anorthite–diopside–titanite system (Shosnig and Hoffer, 1998) and silicate melt–titanite partition coefficients for five different melt compositions of ASI (molar ratio $Al_2O_3/(Na_2O + K_2O + CaO)$) = 0.59*, 0.64, 0.76 and 0.77 (Prowatke and Klemme, 2005). (b) PM-normalized trace element patterns for titanite in the leucogranite and possible titanite-forming melt. Melt compositions are calculated using silicate melt–titanite partitioning data for ASI = 0.59*, 0.64, 0.76 and 0.77 (Prowatke and Klemme, 2005). *—two partition coefficient data.

Figure 9. A P–T diagram showing estimated titanite formation temperatures and metamorphic condition of the Hida Belt in the literature (Suzuki et al., 1989). This figure also shows titanite isopleths as a function of both temperature and pressure calculated using the experimental calibration of Hayden et al. (2008). The titanite formation temperatures were estimated using Zr-in-titanite thermometry (Hayden et al., 2008) and calculated the TiO_2 activity for 0.5 and 1 at nominal pressure conditions of 0.4–0.7 GPa. Wet pelitic solidus, diorite solidus and low-pressure limit of Fe-staurolite are after Thompson (1982), Palin et al. (2016) and Richardson (1968), respectively.

Figure 10. Summary of geochronological studies in the Hida Belt. Magmatic*—magmatic zircons ages including inherited core, detrital grains and unclear interpretation; Magmatic**—zircon ages of younger granite. References are shown in Supplementary material 1.

Table 1

Spot ID	^{207}Pb/^{235}U	2σ	^{206}Pb/^{238}U	2σ	^{207}Pb/^{206}Pb	2σ	^{235}U/^{207}Pb age	2σ	^{238}U/^{206}Pb age	2σ	^{207}Pb/^{206}Pb age	2σ
1-2-1	1.16	0.0402	0.0430	0.00140	0.195	0.00239	779.9	18.9	271.7	8.7	2782.4	20.1
1-2-2	1.39	0.0484	0.0451	0.00147	0.224	0.00275	885.5	20.6	284.3	9.1	3009.0	19.7
1-2-3	1.19	0.0413	0.0439	0.00143	0.197	0.00240	795.4	19.2	276.7	8.8	2798.1	20.0
1-2-5	1.30	0.0462	0.0457	0.00149	0.207	0.00285	846.9	20.4	287.8	9.2	2881.7	22.4
1-2-6	1.38	0.0491	0.0454	0.00148	0.221	0.00307	881.8	20.9	286.0	9.1	2988.9	22.3
1-2-7	1.04	0.0361	0.0422	0.00137	0.179	0.00216	724.3	18.0	266.2	8.5	2644.4	20.0
1-2-8	1.29	0.0460	0.0435	0.00142	0.215	0.00306	842.1	20.4	274.5	8.8	2946.1	22.9
1-2-9	1.37	0.0492	0.0461	0.00151	0.215	0.00317	876.3	21.1	290.8	9.3	2946.4	23.8
1-2-10	1.58	0.0564	0.0457	0.00150	0.250	0.00359	961.8	22.2	288.4	9.2	3186.5	22.7
1-2-11	1.38	0.0485	0.0450	0.00147	0.223	0.00290	880.8	20.7	283.5	9.0	3000.6	20.9
1-2-12	1.73	0.0613	0.0479	0.00157	0.262	0.00358	1019.4	22.8	301.4	9.6	3258.9	21.5
1-2-13	1.57	0.0555	0.0466	0.00152	0.244	0.00331	957.9	21.9	293.7	9.4	3146.9	21.6
1-2-14	1.30	0.0463	0.0445	0.00146	0.212	0.00298	846.2	20.4	281.0	9.0	2919.6	22.8
1-2-15	1.52	0.0539	0.0470	0.00154	0.235	0.00320	939.2	21.7	296.0	9.5	3085.5	21.7
1-3-1	1.28	0.0423	0.0447	0.00137	0.207	0.00253	836.1	18.8	281.9	8.5	2885.2	19.8
1-3-2	1.27	0.0418	0.0444	0.00136	0.207	0.00250	831.2	18.7	279.9	8.4	2883.2	19.6
1-3-3	1.90	0.0618	0.0493	0.00151	0.279	0.00306	1079.9	21.7	310.1	9.3	3358.2	17.1
1-3-4	1.52	0.0509	0.0476	0.00147	0.232	0.00301	938.7	20.5	299.6	9.0	3064.4	20.8
1-3-5	1.55	0.0507	0.0469	0.00144	0.240	0.00270	950.9	20.2	295.5	8.9	3119.0	17.9
1-3-6	1.60	0.0524	0.0475	0.00146	0.245	0.00275	970.7	20.4	299.0	9.0	3150.3	17.9
1-3-7	1.67	0.0547	0.0482	0.00148	0.251	0.00288	995.8	20.8	303.2	9.1	3190.7	18.1
1-3-8	3.86	0.124	0.0668	0.00205	0.419	0.00396	1606.1	25.9	417.1	12.4	3979.5	14.1
1-3-9	1.50	0.0493	0.0455	0.00140	0.239	0.00278	930.6	20.0	286.9	8.6	3114.2	18.5
1-3-10	1.11	0.0369	0.0417	0.00128	0.194	0.00242	759.0	17.7	263.2	7.9	2772.2	20.5
1-3-11	1.27	0.0425	0.0448	0.00138	0.205	0.00273	830.4	19.0	282.3	8.5	2866.8	21.7
1-3-12	1.28	0.0428	0.0443	0.00137	0.209	0.00277	835.2	19.1	279.4	8.4	2897.6	21.5
1-3-13	1.24	0.0420	0.0442	0.00136	0.204	0.00283	819.4	19.0	278.8	8.4	2855.4	22.6
1-3-14	2.13	0.0709	0.0504	0.00156	0.306	0.00380	1158.3	23.0	317.2	9.6	3501.9	19.2
1-3-15	1.65	0.0552	0.0484	0.00149	0.247	0.00323	988.3	21.2	304.5	9.2	3165.0	20.8
1-1-1	1.12	0.0252	0.0422	0.00077	0.193	0.00253	764.9	12.0	266.3	4.7	2770.3	21.5
1-1-2	1.29	0.0285	0.0437	0.00079	0.215	0.00268	842.5	12.6	275.6	4.9	2940.9	20.2
1-1-3	1.10	0.0246	0.0431	0.00078	0.186	0.00241	755.4	11.9	272.3	4.8	2703.9	21.4
1-1-4	1.12	0.0248	0.0427	0.00077	0.191	0.00241	765.2	11.9	269.5	4.8	2751.4	20.7
1-1-5	1.19	0.0263	0.0432	0.00078	0.199	0.00253	795.2	12.2	272.8	4.8	2821.3	20.7
1-1-6	1.18	0.0263	0.0433	0.00079	0.198	0.00252	793.5	12.2	273.5	4.9	2811.9	20.8
1-1-7	1.22	0.0273	0.0436	0.00079	0.203	0.00263	810.3	12.5	275.4	4.9	2849.7	21.1
1-1-8	1.28	0.0283	0.0437	0.00079	0.213	0.00267	837.9	12.6	275.8	4.9	2926.6	20.3
1-1-9	1.67	0.0366	0.0477	0.00087	0.254	0.00310	997.2	13.9	300.1	5.3	3210.6	19.3
1-1-10	1.25	0.0270	0.0434	0.00078	0.209	0.00250	822.3	12.2	273.6	4.8	2895.3	19.4
1-1-11	1.57	0.0343	0.0466	0.00085	0.245	0.00296	958.6	13.5	293.5	5.2	3149.5	19.2
1-1-12	1.19	0.0266	0.0431	0.00078	0.200	0.00261	796.8	12.3	272.2	4.8	2829.9	21.2
1-1-13	1.34	0.0300	0.0450	0.00082	0.217	0.00279	864.7	13.0	283.6	5.1	2955.9	20.8
1-1-14	1.15	0.0272	0.0439	0.00081	0.190	0.00282	778.4	12.8	277.2	5.0	2744.0	24.4
1-1-15	1.30	0.0293	0.0443	0.00081	0.212	0.00282	843.8	12.9	279.5	5.0	2921.5	21.5
1-4-1	1.53	0.0396	0.0463	0.00109	0.240	0.00255	942.8	15.9	292.0	6.7	3117.2	16.9
1-4-2	1.18	0.0310	0.0438	0.00103	0.195	0.00228	790.8	14.5	276.1	6.4	2788.1	19.1
1-4-3	1.17	0.0320	0.0447	0.00106	0.191	0.00257	788.0	15.0	281.6	6.5	2746.5	22.2
1-4-4	1.16	0.0314	0.0441	0.00105	0.191	0.00248	783.2	14.7	278.4	6.5	2751.1	21.3
1-4-5	1.17	0.0317	0.0439	0.00104	0.192	0.00255	784.5	14.8	277.1	6.4	2763.0	21.7
1-4-6	1.01	0.0265	0.0423	0.00100	0.172	0.00205	706.6	13.4	267.3	6.2	2579.7	19.8
1-4-7	1.18	0.0312	0.0447	0.00106	0.192	0.00226	792.1	14.5	282.2	6.5	2755.5	19.4
1-4-8	1.20	0.0327	0.0457	0.00108	0.191	0.00253	801.5	15.1	288.0	6.7	2748.8	21.8
1-4-9	1.36	0.0360	0.0469	0.00111	0.210	0.00253	871.3	15.5	295.3	6.8	2907.1	19.5
1-4-10	1.35	0.0349	0.0456	0.00107	0.214	0.00232	866.3	15.1	287.6	6.6	2937.3	17.5
1-4-11	3.03	0.0763	0.0603	0.00142	0.365	0.00327	1416.3	19.2	377.4	8.6	3770.6	13.6
1-4-12	1.60	0.0413	0.0485	0.00114	0.240	0.00251	971.1	16.1	305.4	7.0	3117.0	16.7
1-4-13	1.63	0.0434	0.0489	0.00116	0.242	0.00291	983.3	16.7	307.7	7.1	3135.7	19.1
1-4-14	1.34	0.0364	0.0461	0.00109	0.210	0.00279	861.6	15.8	290.3	6.7	2908.8	21.5
1-4-15	1.36	0.0368	0.0464	0.00110	0.213	0.00276	872.8	15.8	292.6	6.8	2926.7	20.9
1-5-1	1.35	0.0385	0.0456	0.00121	0.214	0.00228	865.9	16.7	287.6	7.5	2936.0	17.2
1-5-2	1.49	0.0425	0.0464	0.00123	0.234	0.00237	928.0	17.3	292.4	7.6	3076.3	16.2
1-5-3	1.52	0.0435	0.0476	0.00127	0.232	0.00245	939.0	17.5	300.1	7.8	3062.8	16.9
1-5-4	1.21	0.0346	0.0439	0.00117	0.199	0.00219	802.9	16.0	276.7	7.2	2820.4	17.9
1-5-5	1.42	0.0407	0.0459	0.00122	0.225	0.00238	897.8	17.1	289.1	7.5	3014.9	17.0
1-5-6	1.29	0.0370	0.0447	0.00119	0.209	0.00230	840.2	16.4	281.7	7.3	2898.4	17.8
1-5-7	1.24	0.0367	0.0448	0.00120	0.201	0.00252	820.3	16.6	282.6	7.4	2835.8	20.4
1-5-8	1.30	0.0384	0.0455	0.00122	0.207	0.00262	844.5	17.0	287.0	7.5	2879.3	20.6
1-5-9	1.22	0.0362	0.0446	0.00119	0.198	0.00258	808.5	16.6	281.5	7.4	2807.6	21.3
1-5-10	1.25	0.0362	0.0444	0.00118	0.204	0.00231	823.7	16.3	279.9	7.3	2861.8	18.4
1-5-11	1.48	0.0425	0.0461	0.00123	0.233	0.00251	921.6	17.4	290.4	7.6	3070.7	17.3
1-5-12	1.77	0.0504	0.0489	0.00130	0.263	0.00262	1036.0	18.4	308.0	8.0	3264.0	15.7
1-5-13	1.33	0.0383	0.0439	0.00117	0.220	0.00241	859.6	16.7	277.0	7.2	2980.7	17.6
1-5-14	2.16	0.0606	0.0532	0.00141	0.294	0.00272	1167.4	19.5	334.3	8.6	3438.8	14.3
1-5-15	3.44	0.0952	0.0631	0.00167	0.395	0.00313	1513.8	21.8	394.5	10.1	3891.7	11.9

Figure 1 [1-page width]

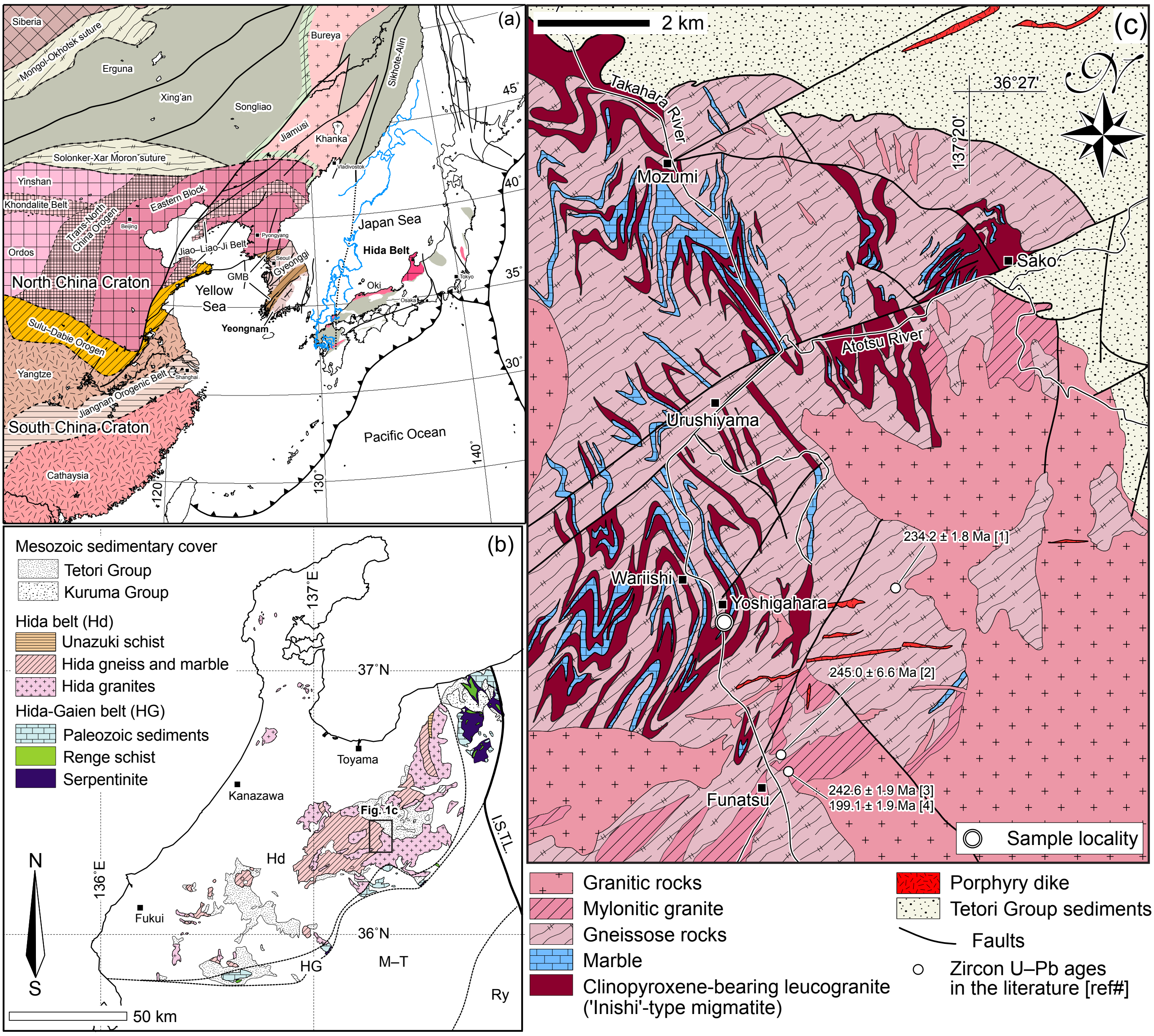

Figure 2 [1-page width]

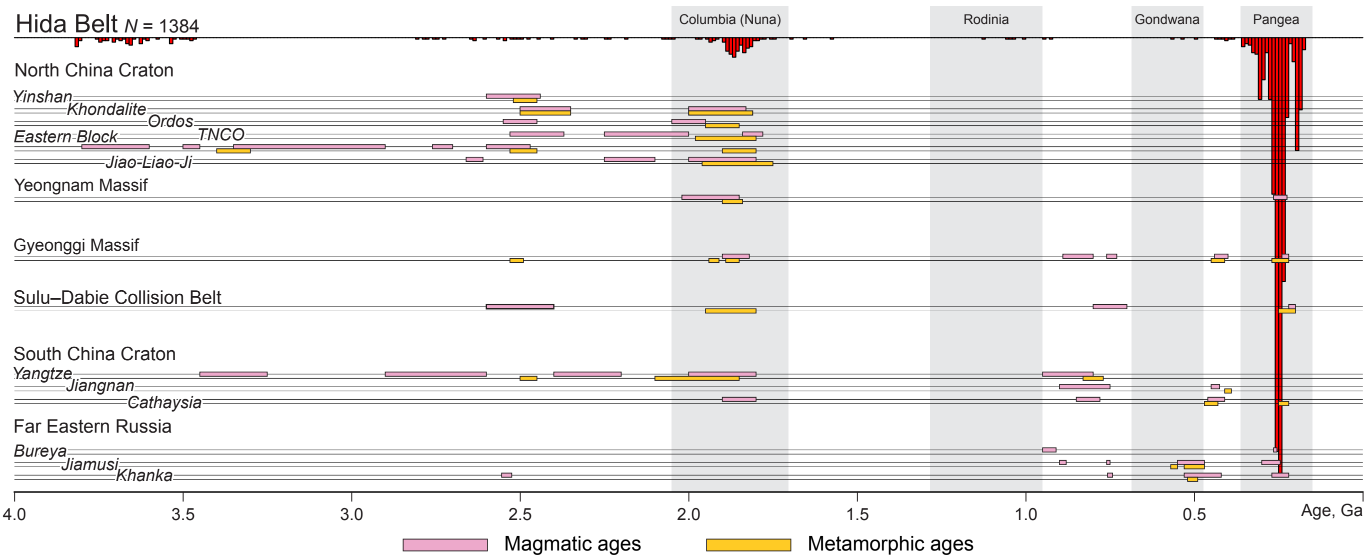

Figure 3 [1-page width]

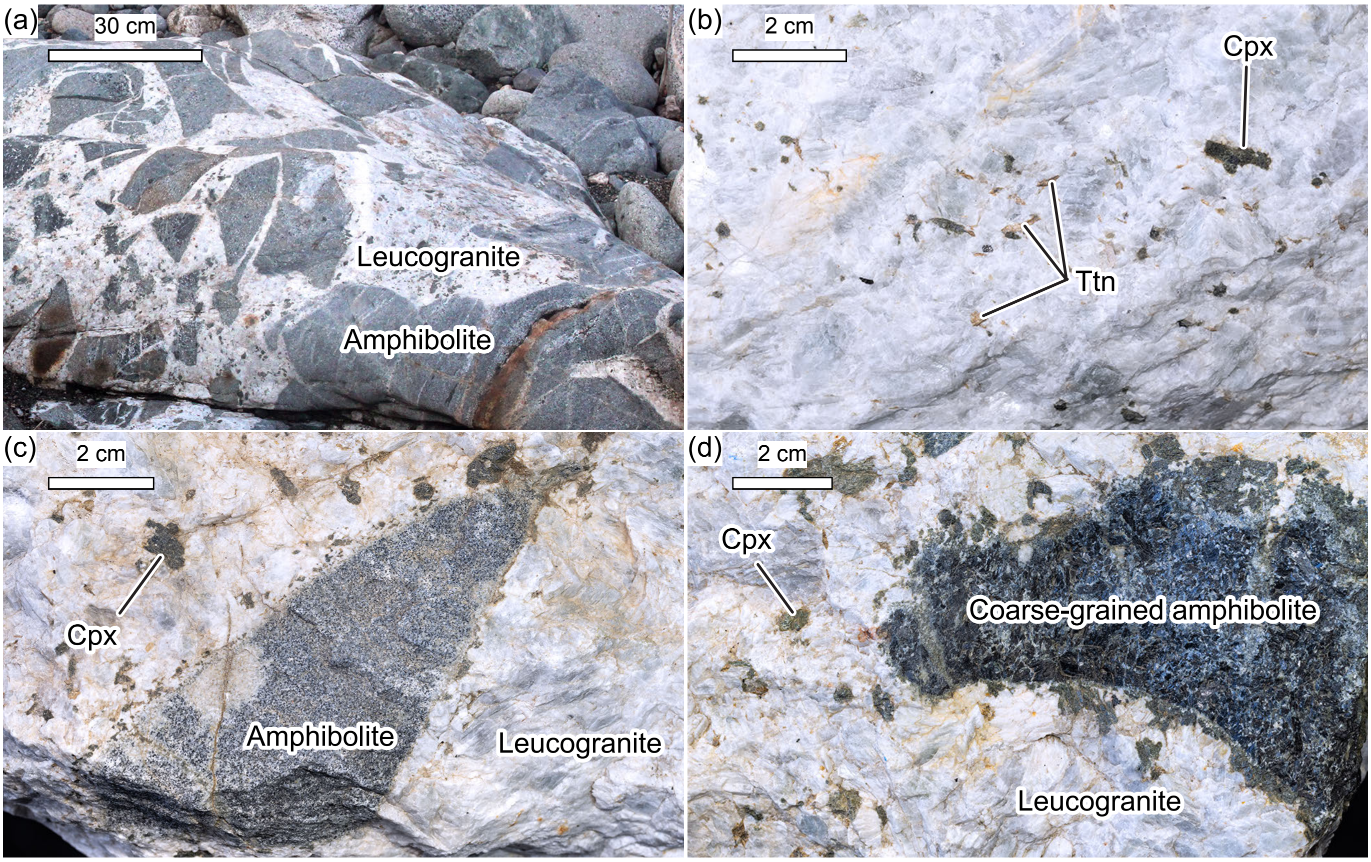

Figure 4 [1-page width]

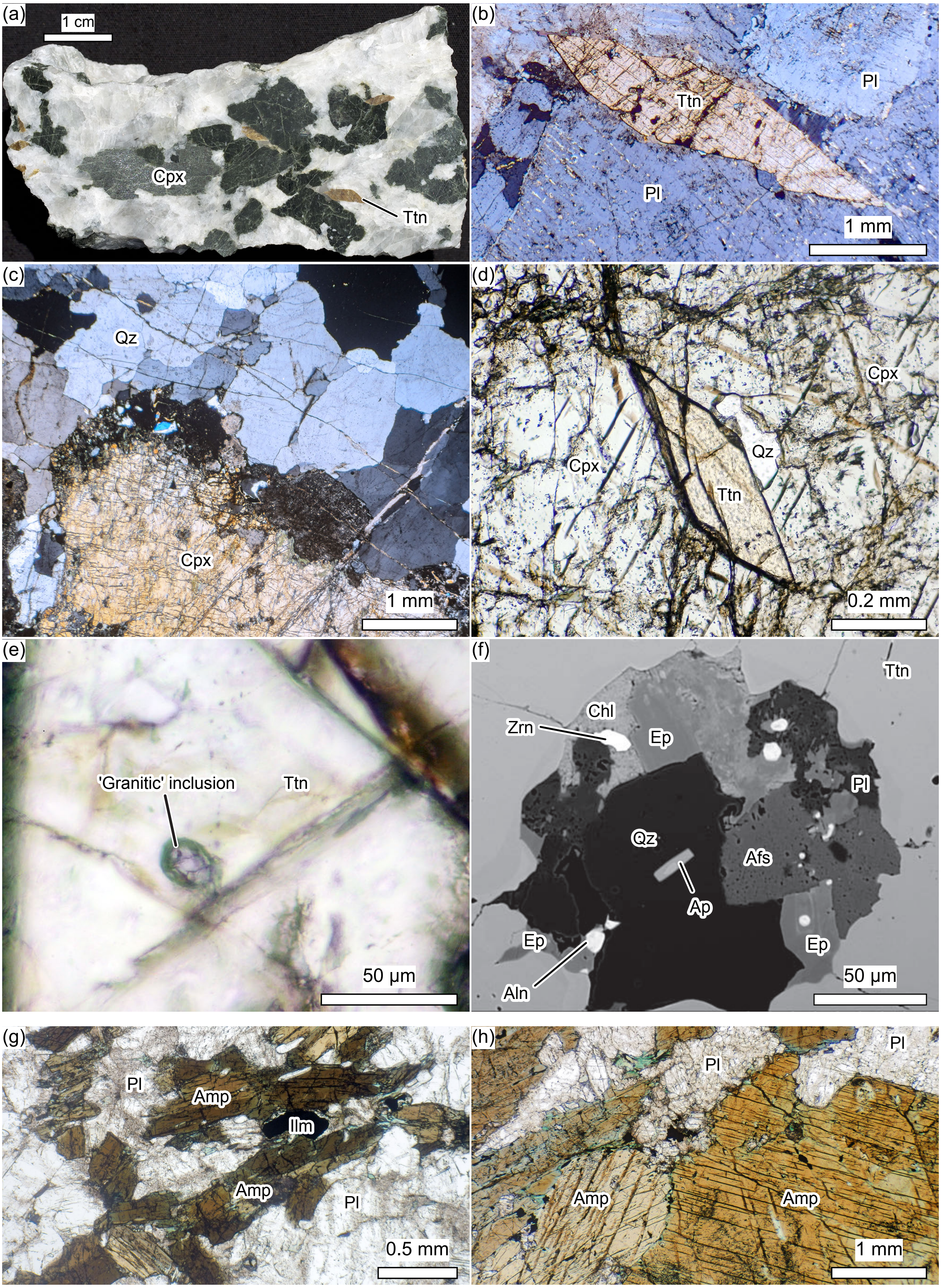

Figure 5 [1-column width]

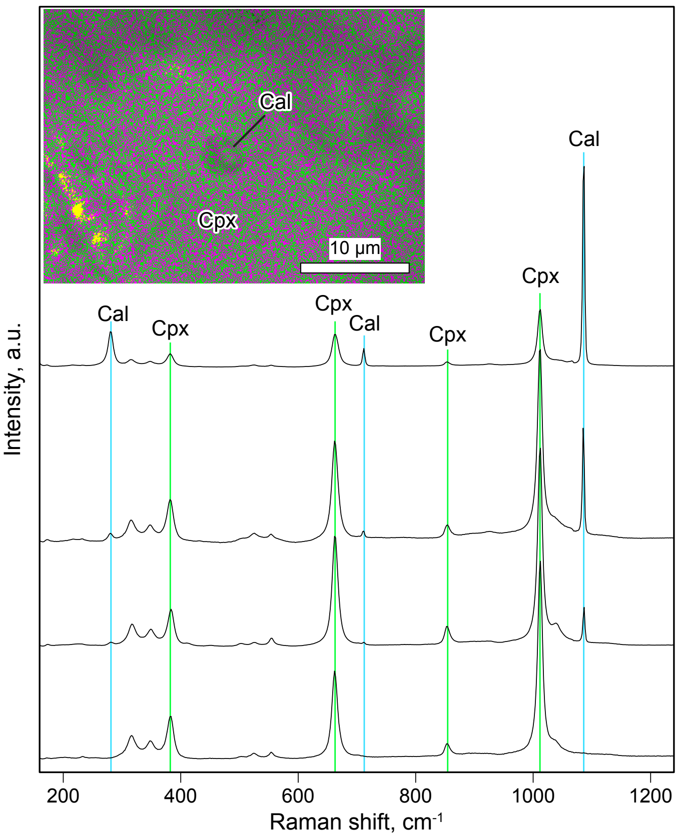

Figure 6 [1-page width]

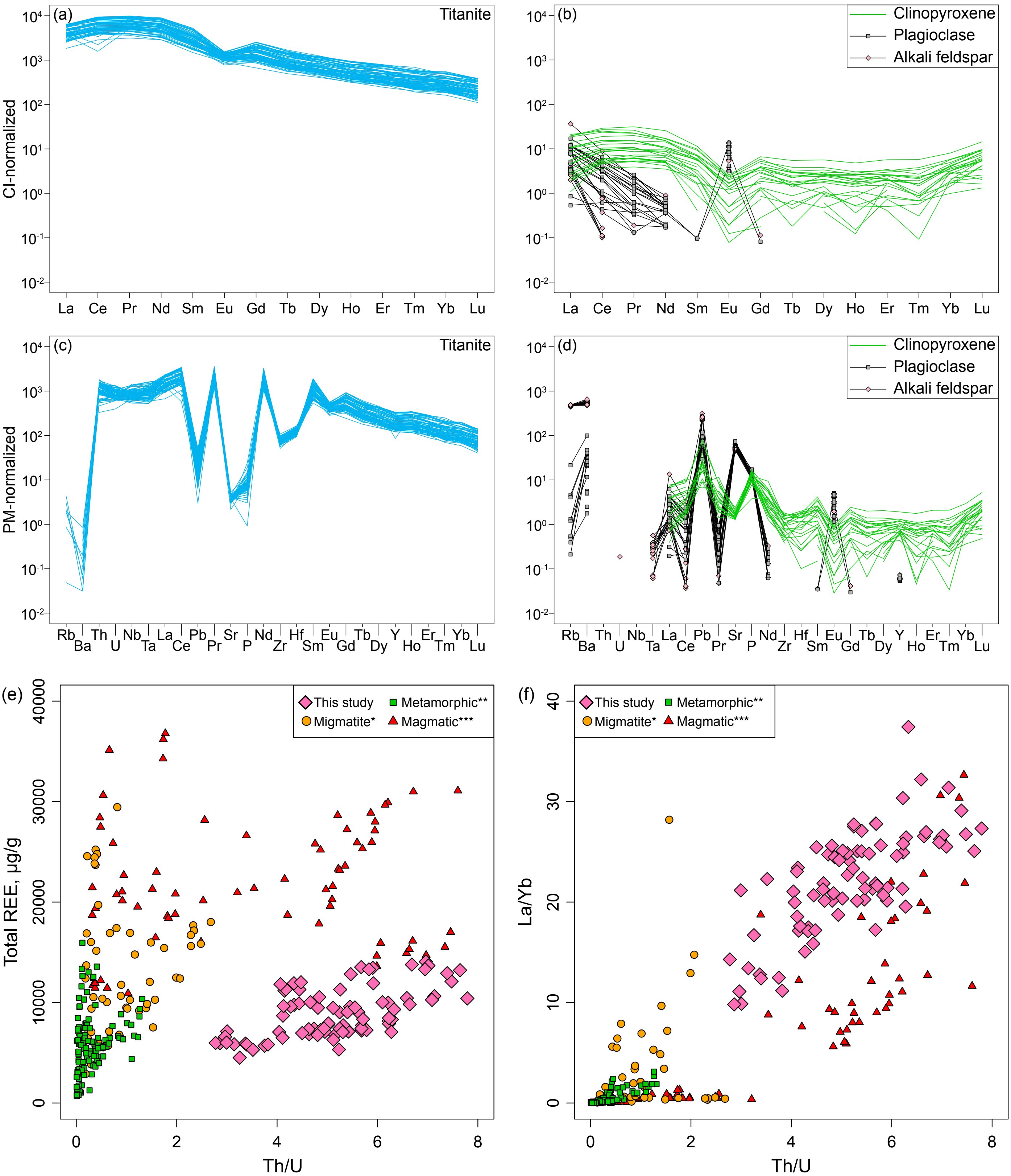

Figure 7 [1-column width]

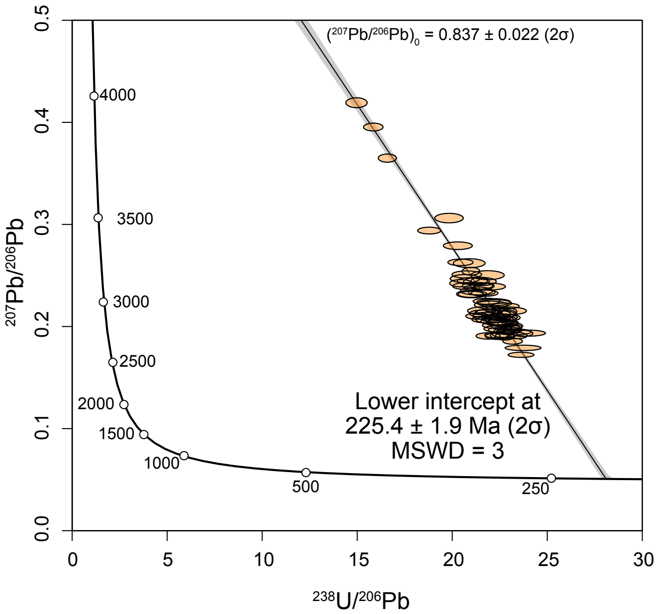

Figure 8 [1-column width]

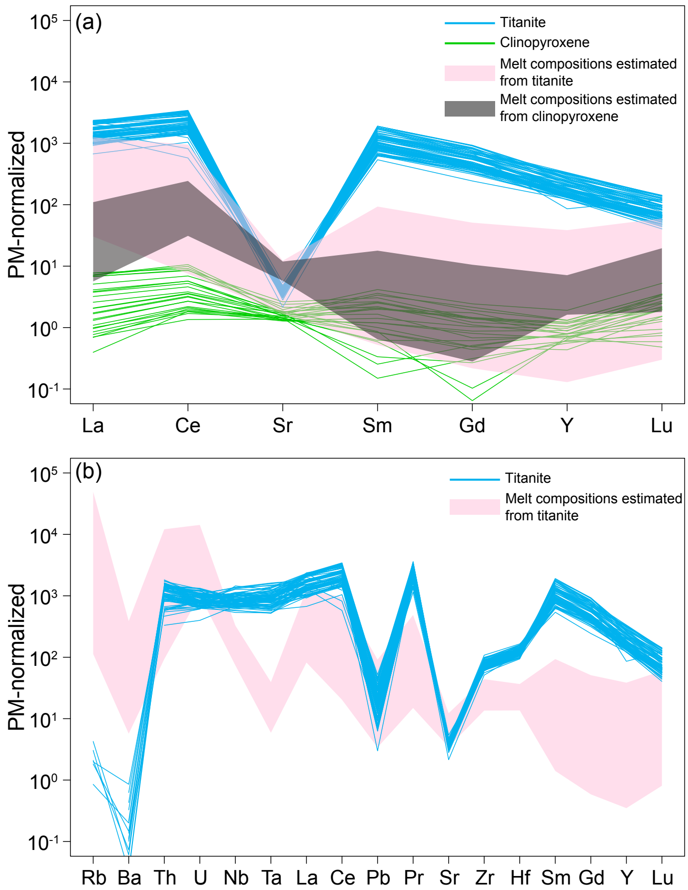

Figure 9 [1-column width]

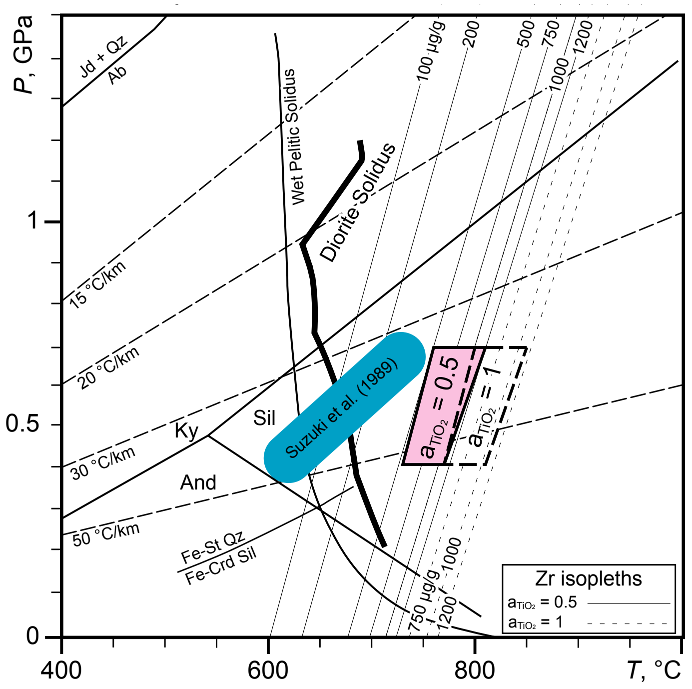

Figure 10 [2/3 page width]